Driven Topological Transitions in Active Nematic Films

Soft Matter

ARTICLE TYPE

Cite this: DOI: 00.0000/xxxxxxxxxx

Driven Topological Transitions in Active Nematic Films†

David P. Rivas,[a] Tyler N. Shendruk,[b,c], Robert R. Henry[a], Daniel H. Reich[a], and Robert L. Leheny*[a]

Received Date
Accepted Date

DOI: 00.0000/xxxxxxxxxx

The topological properties of many materials are central to their behavior. In intrinsically out-of-equilibrium active materials, the dynamics of topological defects can be particularly important. In this paper, local manipulation of the order, dynamics, and topological properties of microtubule-based active nematic films is demonstrated in a joint experimental and simulation study. Hydrodynamic stresses created by magnetically actuated rotation of disk-shaped colloids in proximity to the films compete with internal stresses in the active nematic, influencing the local motion of $+1/2$ charge topological defects that are intrinsic to the nematic order in the spontaneously turbulent active films. Sufficiently large applied stresses drive the formation of $+1$ charge topological vortices through the merger of two $+1/2$ defects. The directed motion of the defects is accompanied by ordering of the vorticity and velocity of the active flows within the film that is qualitatively unlike the response of passive viscous films. Many features of the film's response to the stress are captured by Lattice Boltzmann simulations, providing insight into the anomalous viscoelastic nature of the active nematic. The topological vortex formation is accompanied by a rheological instability in the film that leads to significant increase in the flow velocities. Comparison of the velocity profile in vicinity of the vortex with fluid-dynamics calculations provides an estimate of the film viscosity.

1 Introduction

Topological defects in the ordered states of physical systems can play critical roles in determining their properties. In condensed matter, examples include magnetic flux lines penetrating type-II superconductors, dislocations in crystalline solids, and singular regions in the magnetization of ferromagnetic thin films[1–3]. These structures, which possess a conserved topological charge, have non-local effects on the order within the systems, whose dynamics can often be described in terms of the defects' quasi-particle-like motion and interactions. Further, the ability to control defect behavior is essential for applications.

Particularly intriguing topological defect dynamics occur in active nematic films, which are quasi-two-dimensional (2D) fluids composed of rod-like constituents that possess the orientational order of nematic liquid crystals but flow spontaneously due to an internal energy source[4–6]. Examples include cell cultures[7–11], bacteria suspensions[12–16], granular media[17], and engineered systems composed of dense solutions of microtubule or actin biopolymers adsorbed at oil-water interfaces and driven by molecular motors[18,19]. In the microtubule films, the local orientation of the microtubules defines the nematic director field $\mathbf{n}(\mathbf{r})$. Activity induced by the molecular motors causes the microtubules to slide along one another, creating extensional strains that drive bend instabilities in $\mathbf{n}(\mathbf{r})$ that lead to the perpetual creation and annihilation of pairs of defects with topological charges $\pm 1/2$. The extensional strains further propel the $+1/2$ defects, leading to striking, turbulence-like flows[20–22].

In the case of traditional liquid crystals, much of the technological importance derives from the ability to address and reconfigure the order locally and dynamically through a combination of patterned boundary conditions and applied fields. Progress toward achieving comparable manipulation of active nematics requires control of the dynamic defects. Recent experiments have demonstrated passive approaches to affect defect behavior via spatially resolved alignment of the director through confining boundary conditions[23–25] that can be considered analogous to surface anchoring. However, the ability to couple actively and tunably to local active nematic behavior, and to defect motion in particular, through applied fields has not been realized. Here, we report combined experiments and simulations in which we demonstrate and model local, dynamic influence over the flow properties and director field structure in active nematic films through stress fields

[a] Department of Physics and Astronomy, Johns Hopkins University, Baltimore, MD, USA, 21218
[b] Interdisciplinary Centre for Mathematical Modelling and Department of Mathematical Sciences, Loughborough University, Loughborough, UK, LE11 3TU
[c] School of Physics and Astronomy, The University of Edinburgh, Edinburgh, UK, EH9 3FD.

† Electronic Supplementary Information (ESI) available.

* Email: leheny@jhu.edu.

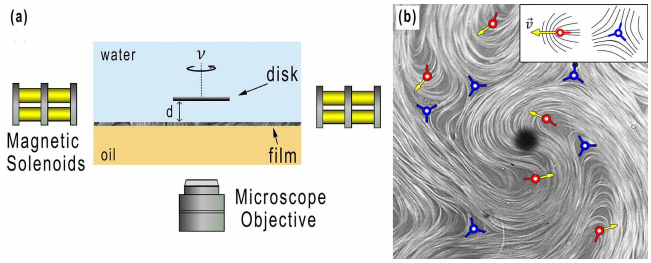

Fig. 1 Experimental design for imposing stress locally on active nematic films. (a) A 40-μm-diameter ferromagnetic Ni disk positioned a height $d = 15-40$ μm above a film is rotated at a frequency ν by a magnetic field created by a set of four pairs of solenoids (two shown) mounted an inverted fluorescence microscope. (b) Example image of a disk rotating counterclockwise above a film composed of fluorescently labeled microtubule bundles. The nematic film is populated with $-1/2$ (blue) and $+1/2$ (red) topological defects. The instantaneous velocities of the mobile $+1/2$ defects are indicated by the yellow arrows, and their orientation vectors are indicated by red arrows.

created by rotating disk-shaped colloids in proximity to the films. The hydrodynamic stresses produced by the disks alter the behavior of the active nematic by steering the motion of the topological defects, which allows us to infer anomalous viscoelastic properties of the active films. Most notably, we find that above a threshold applied stress, a rotating disk can entrain two $+1/2$ defects and induce their fusion into a single vortex structure with topological charge $+1$. In overcoming the innate repulsion between like-charged topological objects, which ordinarily is a critical determining factor in the dynamics of multi-defect states, this defect merger illustrates the degree of control of topological properties that can be achieved in active systems.

2 Materials and Methods

Active nematic films, composed of a dense layer of fluorescent microtubule bundles driven by kinesin molecular motors, were formed at oil-water interfaces[18] using materials provided by the Brandeis University Materials Research Science and Engineering Center Biological Materials Facility, as detailed in Section II of the SI. As part of the film formation, 40-μm-diameter ferromagnetic nickel disks, introduced into the aqueous phase, became positioned at a height $d =$ 3-8 μm above the film with the disk faces parallel to the film. This height appeared to be set by a thin, dilute layer of unadsorbed microtubules adjacent to the film upon which the disks rested.

Observations of the disks and films were made on an inverted microscope (Nikon TE2000) using a Flare CameraLink camera (IOIndustries), as described in the SI. Four pairs of solenoids mounted on the microscope[26] generated rotating magnetic fields of specified magnitude and frequencies up to $\nu =$ 120 Hz in the plane of the film. A schematic of the experiment is given in Fig. 1a. The magnetic moments of the disks lie in the disk plane, hence the magnetic torque from the applied fields caused the disks to rotate about their axes also at frequency ν. When rotated, the disks rose to a greater height above the film. For instance, at $\nu =$ 80 Hz, the disks typically reached $d =$ 15-40 μm. We identify this rise with a possible normal force due to the non-Newtonian character of the dilute suspension of unadsorbed microtubules between the disk and film[27]. Figure 1b shows an image of a rotating disk above an active nematic film where the $+1/2$ and -1/2 defects are labeled. The orientation vectors $\hat{\psi}$ of the $+1/2$ defects[28,29] and the directions of the instantaneous velocities of their self-propelled motion, which is approximately antiparallel to $\hat{\psi}$, are further indicated.

3 Results

3.1 Topological vortex formation and decay.

When the applied magnetic field was zero and the disk was not rotating, it had no observable effect on the active nematic; however, the disk was carried along with the flow of the film, indicating the thin aqueous layer between disk and film provided a strong hydrodynamic coupling between the disk and film. Consequently, when a disk rotated, it imposed significant hydrodynamic stresses on the film, influencing the local nematic order and active flows. A quantitative estimate of the stresses is provided in the SI. Above a threshold ν, typically 60-120 Hz, the stresses were sufficient to drive topological transitions in the nematic order, wherein topological vortices with $+1$ topological charge were created from the fusion of two $+1/2$ defects. Figure 2 shows a series of images of a film during creation of a topological vortex (see Supplementary Video S1). Since total topological charge must be conserved, vortex creation necessitated a change in the total topological charge of the population of 1/2-charged defects existing in the film. For instance, in Fig. 2, two $+1/2$ and -1/2 defect pairs are created in the vicinity of the disk (Figs. 2b and c). The $+1/2$ defects spiral inward toward the disk until they merge to form the $+1$ vortex defect (Fig. 2e), leaving the -1/2 defects behind to eventually annihilate with other $+1/2$ defects in the film. The vicinity of the rotating disk was a frequent location for formation of 1/2-charged defect pairs, likely due to the tendency of the director to align azimuthally in response to the external flow coupled with the hydrodynamic bend instability of the active nematic[30,31], and hence formation of topological vortices commonly involved the merger of $+1/2$ defects that were created near the disk as in Fig. 2. However, the $+1/2$ defects involved in topological vortex formation sometimes originated far from the disk and became captured as they passed in proximity to the disk.

To explore further the merger of $+1/2$ defects into a topological object of charge $+1$, we conducted simulations of active nematic films coupled to rotating disks by solving the Beris-Edwards formulation of nematohydrodynamics, employing a Lattice-Boltzmann (LB) algorithm for the flow field and finite difference for the orientation tensor[32–35]. Details regarding the simulations are provided in the SI. Simulation parameters were chosen to optimize agreement with spatial and temporal correlations in vorticity in the experiments, thereby setting the length and time scales for the simulation. The disk in the simulations was subjected to a constant torque to drive rotation. The coupling between disk and active nematic film, which we interpret as a viscous coupling through the thin aqueous layer between disk

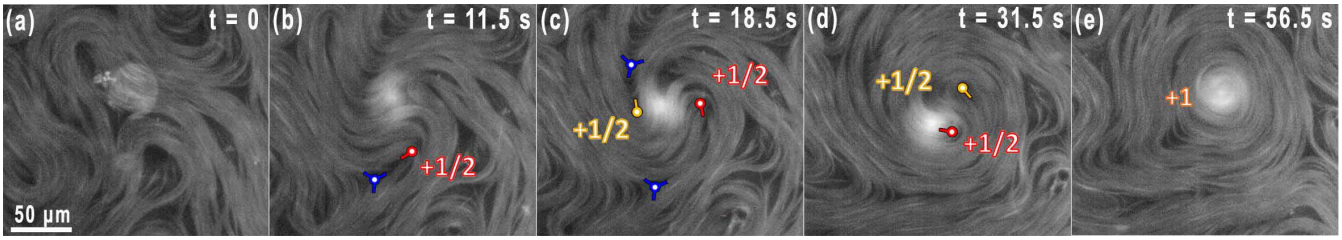

Fig. 2 Fluorescence micrographs showing topological vortex formation in an active nematic film. (a) A non-rotating disk (bright circle) sits atop the active nematic film just prior to application of a magnetic field rotating at 80 Hz. (b) A $\pm 1/2$ defect pair is created in proximity to the disk. (c) A second $\pm 1/2$ defect pair forms near the disk, while the stresses imposed by the disk cause the positive defects to orient and circle the disk. (d) The $+1/2$ defects spiral in towards the disk center. (e) The two $+1/2$ defects fuse to form a $+1$ topological vortex, thus conserving the overall charge of the system.

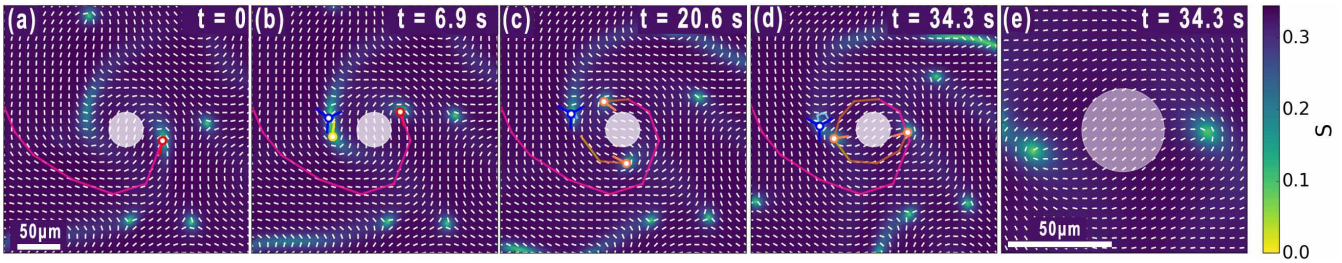

Fig. 3 Simulation of the merger of two $+1/2$ defects into a $+1$ topological structure by a rotating disk. (a) A $+1/2$ defect (trajectory in red) begins circling the disk. (b) A defect pair is created near the disk. (c) The two $+1/2$ defects circle the disk. (d) The $+1/2$ defects orient in a radial manner to create a metastable bound state. (e) Magnified view of the $+1$ topological structure in panel d. The white lines display the director field and the color map indicates the scalar order parameter S. The disk-to-film coupling is $\zeta_{\text{d-f}} = 0.03$, and the alignment parameter is $\lambda = 0.3$.

and film in the experiment, was modeled in the simulations by a drag coefficient $\zeta_{\text{d-f}}$, whose magnitude served as a proxy for effective rotation rate. Similarly, the nematic orientation is coupled to velocity gradients within the film by an alignment parameter λ (see SI).

Figure 3 illustrates a defect merger event in a simulation (see Supplementary Video S2) that mirrors the topological vortex formation in the experiments. A $+1/2$ defect was drawn from the surrounding bulk turbulence into orbit about the rotating disk and proceeded to spiral toward the disk with $\hat{\psi}$ oriented azimuthally (Fig. 3a). A second $+1/2$ defect appeared in the vicinity of the disk by a pair creation event (Fig. 3b), and the two $+1/2$ defects began orbiting the disk on opposites sides from each other. As they orbited, the defects re-oriented so that each $\hat{\psi}$ pointed radially inward thereby forming a bound pair that constituted a $+1$ topological complex (Figs. 3c and d). The $+1$ topological objects formed in the experiments and simulations hence differed in their core structure. While in the simulations the core contained two distinguishable $+1/2$ defects linked by a well defined local director field (Fig. 3e), in the experiments the $+1/2$ defects merged fully to form a singular, point-like core like in Fig. 2e (see also Fig. 4a below). As described below, ~~W~~we ~~identify~~ hypothesize that the complete merger in the experiments ~~with~~ is a consequence of a nonlinear rheological response of the active nematic films ~~described below~~.

Such fusion of like-charge topological defects as in Fig. 2 is unusual in nature. Like-charge defects typically interact through long-range repulsion[28,29]. Furthermore, a $+1$ topological vortex in a nematic has higher energy than two $+1/2$ defects[36], so the merger requires input of energy, While these restrictions make such defect mergers rare in passive liquid crystals, the internal energy source driving the flows in active nematics can under appropriate conditions, such as under confinement[24], facilitate defect merger. We see further here how locally applied external fields, in this case hydrodynamic stresses, in conjunction with the activity can drive defect mergers.

As high-energy quasi-particles, the topological vortices were susceptible to decay. Further, since deformations of the director field in the vicinity of the $+1$ defect are pure bend, sustaining the configuration required suppressing the hydrodynamic instability intrinsic to the active nematic films that drives flow normal to the director in regions of bend and leads to amplification of the bend distortion[30,31]. In the experiments, the stresses from the rotating disk could nevertheless stabilize the $+1$ defect for extended periods, longer than 6 minutes in one measurement, a time scale far exceeding the intrinsic correlation time of the active nematic, which was approximately 30 s (see SI). However, fluctuations in the disk position or local nematic order would eventually lead the vortex to decay into a pair of lower-energy $+1/2$ defects that then propagated away from one another (Figs. 4a-d and Supplementary Video S3). The $+1$ topological structures in the simulations decayed similarly (Figs. 4e-h and Supplementary Video S4). The lifetimes of the $+1$ topological objects in the simulations depended on the alignment parameter λ. Increasing the parameter from $\lambda = 0.3$ into the flow aligning regime, $\lambda = 0.7$, decreases the rate of topological vortex decay events for $\zeta_{\text{d-f}} = 0.03$. If either the coupling is increased to $\zeta_{\text{d-f}} = 0.07$ or the alignment is increased to $\lambda = 0.9$, only a single merger event is observed and the resulting

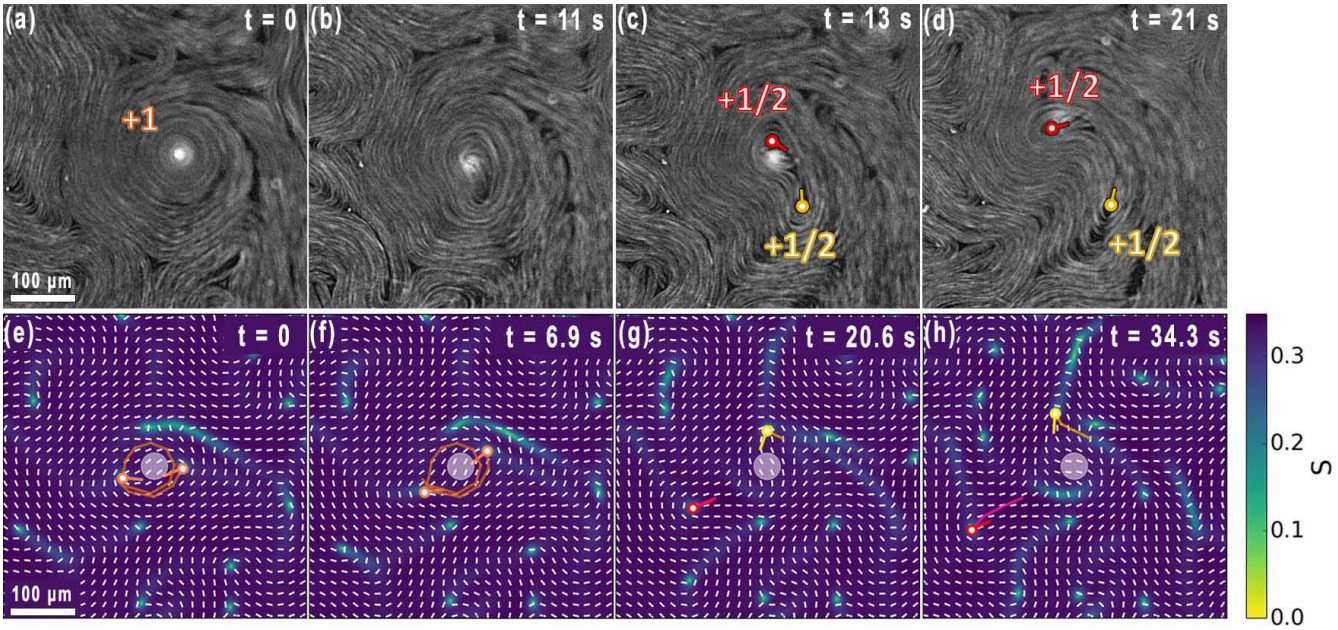

Fig. 4 Topological vortex decay. (a-d) Fluorescence micrographs showing the +1 topological structure dividing into two +1/2 defects that then propagate away from each other. (a) shows a +1 topological vortex created by a rotating disk (seen as a bright spot in the image). (b) shows the initial instability of the azimuthally oriented director about the vortex. A short time later in (c), two clearly separated +1/2 defects are apparent. In (d) the defects continue to propagate away from each other. (e-h) Simulations (with $\zeta_{\text{d-f}} = 0.03$ and $\lambda = 0.3$.) showing the decay of a +1 topological structure. The white lines in (e-h) display the director field and the color map indicates the scalar order parameter S.

+1 topological structure persists for the duration of the simulation. The sensitivity of the lifetime to the film parameters in the simulations reflects the coupling of the orientation field to the hydrodynamic stress. As seen in Figs. 3e or 4e, the +1/2 defects in the simulations orient such that the hydrodynamic stresses binding them within the +1 complex must maintain balance with the active stresses that would otherwise propel the +1/2 defects radially outward.

The speed of the +1/2 defects formed in a vortex decay reached their intrinsic, self-propelled speed essentially immediately and showed no dependence on separation, implying any effects of elastic interactions[28,29] between the defects were overwhelmed by their activity-driven motion[37] (see SI). Once a vortex decayed, the stresses from the rotating disk would drive creation of a new vortex, so that the process repeated. The time scale for new vortex formation could vary from a few seconds to upwards of a minute, as dictated by the time to entrain two new +1/2 defects and develop the non-linear, shear-thinned state in the film described below. This variation and the varied lifetimes of the topological vorticies reflect a stochastic element to the process that results from the close contact between the region of the film under strong influence of the disk and the surrounding sea of active turbulence.

This vortex decay into a defect pair is distinct from the behavior observed in other recent experiments on active nematics that tracked the emergence of active turbulence from ordered director fields. In those cases, where the ordering was imposed by passive confinement[24] or was prepared over large areas[38,39], the return to turbulent flow was initiated by bend instabilities intrinsic to the active nematic with a characteristic wave length set by the film properties. In contrast, the +1 defect decay in Fig. 4 has a quasi-particle-like nature in that the decay produces two, clearly identifiable +1/2 point defects that are in close proximity to the parent +1 point defect and that have subsequent trajectories that are easily tracked. We attribute this quasi-particle nature to the ability of the controlled stresses imposed by the disk to strongly and locally alter the active nematic ordering and dynamics.

3.2 Effects of imposed stress on active nematic structure and flow.

In addition to the striking formation of a high-energy +1 topological vortex through defect merger, the hydrodynamic stresses from the rotating disk imposed more subtle effects on the nematic order and active flows. For example, Fig. 5 displays maps of the flows in the vicinity of a disk rotating at 120 Hz during a period in which no +1 topological vortex has formed (see SI for image analysis details). Figure 5a shows the instantaneous velocity field and the magnitude of the instantaneous vorticity, $\vec{\omega} = \vec{\nabla} \times \vec{v}$, in the flow. Active nematics intrinsically possess regions of non-zero flow vorticity[22], and the regions of positive and negative vorticity in Fig. 5a reflect this structure. The instantaneous flows in the simulation show similar structure, as illustrated in Fig. 5b, and further show how the propagating +1/2 defects are accompanied on either side by regions of clockwise and counter-clockwise local vortices in the flow[40]. In fact, in Fig. 5b one sees the two +1/2 defects nearest the center of the disk oriented such that their counter-clockwise flow vortices co-rotate with the flow vorticity created by the disk.

Figures 5c and d display the same quantities averaged over 300

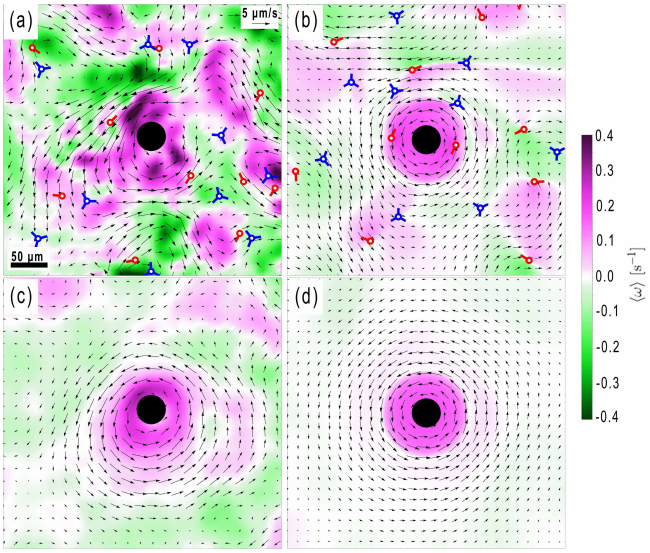

Fig. 5 Instantaneous and time-averaged properties of the active nematic flows. (a) Map of the instantaneous vorticity (color scale) and velocity field (arrows) in an active nematic film in the presence of a disk rotating counterclockwise at 120 Hz. Red and blue markers indicated the $+1/2$ and -1/2 defects, respectively. (b) The same instantaneous quantities taken from LB simulation with coupling $\zeta_{\text{d-f}} = 0.07$ and alignment parameter $\lambda = 0.3$. (c) Map of the vorticity and velocity averaged over 300 s in the experiment. (d) Corresponding time-averaged quantities in the simulation.

seconds. Due to the active turbulence of the flow, the structure at a fixed position ordinarily decorrelates on a time scale of approximately 30 seconds (see SI); so in the absence of the rotating disk, both quantities in Figs. 5c and d would be essentially zero when averaged over 300 seconds. The non-zero values hence illustrate the ability of the stresses from the rotating disk to compete with the active stress and influence locally the flow of the active nematic.

This influence is apparent even at disk rotation rates well below the threshold for creating a topological vortex. For example, Fig. 6 shows a set of quantities characterizing the time-averaged and azimuthally averaged nematic order and flow as a function of distance from the disk center in the absence of a $+1$ topological object. The experimental data is shown for disk rotation rates of both 120 Hz (during periods when no topological vortex forms) and 20 Hz, a rate below the threshold for topological vortex formation. Figure 6a shows the time-averaged flow vorticity which is positive near the disk and negative at intermediate distances. Simulations also show large positive vorticity near the disk and near-zero negative values at larger distance (Fig. 6b). In the simulations, the region of time-averaged negative vorticity is reproduced only when a small drag term[41,42] is included to account for viscous dissipation in the thin oil layer below the film (Fig. 1a), illustrating the importance of such dissipation to the properties of the active flows in experiments[24,43].

Orientational ordering of the defects is shown in Figs. 6c and d, which display the time-averaged and azimuthal-averaged component of the $+1/2$ defect orientation vector $\hat{\psi}$ along the azimuthal direction $\hat{\theta}$ with respect to the disk center. The $+1/2$ defects in close vicinity to the rotating disk tend to orient so that $\langle \hat{\psi} \cdot \hat{\theta} \rangle < 0$, as illustrated in the inset of Fig. 6c, while farther from the disk $\langle \hat{\psi} \cdot \hat{\theta} \rangle > 0$. In the unperturbed active nematic, the extensional flows cause the $+1/2$ defects to move anti-parallel to $\hat{\psi}$. Thus, one might interpret the region with $\langle \hat{\psi} \cdot \hat{\theta} \rangle < 0$ as a tendency for the self-propelled defects to orient in order to co-circulate in the net flow seen in Fig. 5c (see Supplementary Video S5). However, additional LB simulations of rotating disks near passive films and active nematic films with contractile active stresses, in which the direction of self-propelled motion of the $+1/2$ defects flips, also show defects co-circulate in the disk's flow with $\langle \hat{\psi} \cdot \hat{\theta} \rangle < 0$ (see Supplementary Video S6). We hence conclude that the torque orienting a $+1/2$ defect in orbit about the disk is not activity-induced but is related to coupling of $\mathbf{n}(\mathbf{r})$ near the defect with the disk-induced stress field.

We further interpret the region farther from the disk in which $\langle \hat{\psi} \cdot \hat{\theta} \rangle > 0$ as a preference for defects in that region to orient anti-parallel to those closer to the disk since such anti-parallel orientation minimizes the elastic energy of defect interactions[29,44] and allows favorable constructive overlap of the vorticities in the flows around the defects. Indeed, the tendency for near-neighbor $+1/2$ defects in active nematics to align anti-parallel has been observed in simulations [45] and experiment[19] (see also Fig. S3 in the SI). Our simulations in Fig. 6d also show a small, intermediate-distance peak at large effective rotation rates, which represents the slowing of $+1/2$ defects that are oriented such that they move against the disk's counter-clockwise rotation. This peak due to increased sampling of counter-moving defects is not discernible in the experimental data of Fig. 6c.

Figure 6e displays the time-averaged and azimuthal-average speed of the microtubule bundles in the film, which becomes enhanced over the average activity-induced speeds near the disk. The maximum peak beyond the disk radius is reproduced in LB simulations (Fig. 6f) by use of an effective hydrodynamic disk size to account for the effect of the near-disk flows on the film.

Each experimentally measured quantity in Fig. 6 shows similar trends at $\nu = 20$ Hz and 120 Hz; however, the influence of the disk is larger and extends farther at the higher rate, implying this difference in influence is a factor in whether or not the stresses from the rotating disk can drive topological vortex formation. (To set the scale, the nematic correlation length, defined in the SI, is demarcated by the dash-dotted line in Fig. 6.)

3.3 Shear thinning of the active nematic.

Accompanying topological vortex formation, as in Fig. 2, the velocity of the microtubule bundles in the vicinity of the disk increased significantly, as illustrated in Fig. 7, which shows the velocity as a function of distance from the disk center in the presence of a topological vortex and prior to the vortex formation. For reference, the average intrinsic speeds of the microtubules in the film and of the $+1/2$ defects far from the disk due to the activity are shown in Fig. 7 by the horizontal dashed-dotted and dotted lines, respectively. Some enhanced flow might be expected in vicinity to the vortex since the nematic director aligns with the shear flow, which is the orientation in which a nematic typi-

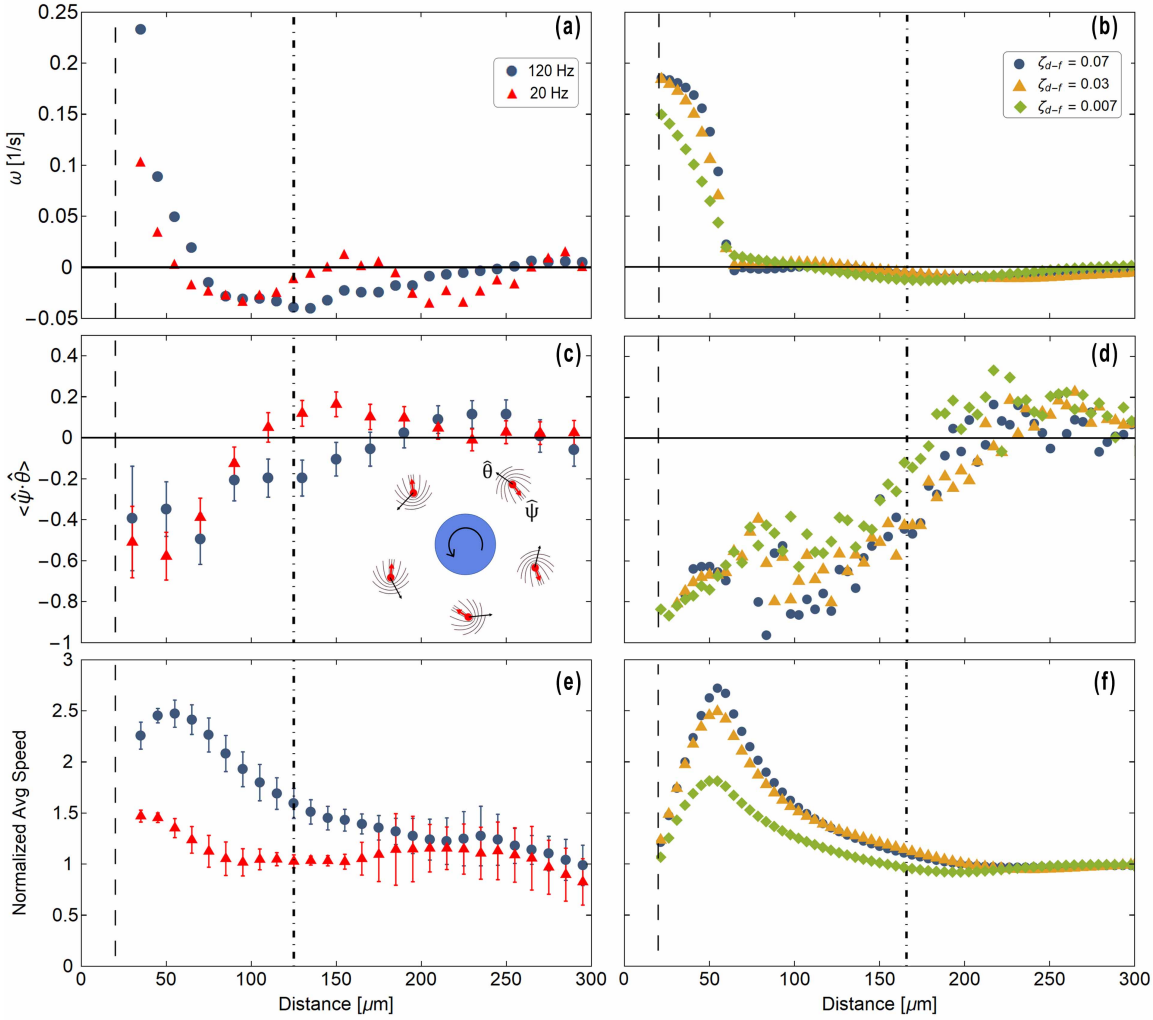

Fig. 6 Characterization of the nematic order and flow in the vicinity of a rotating disk in the absence of a +1 topological vortex. (a) The time and azimuthally averaged vorticity measured in experiment as a function of distance from the disk center at two disk rotation rates. (b) The same quantity obtained in the absence of the +1 topological vortex from simulations at different disk-film couplings. (c) The experimental and (d) the simulated average azimuthal component of the unit orientation vector, $\hat{\psi}$, of the +1/2 defects as a function of distance from the center of a disk. The negative values near the disk indicate a tendency for the defects to circulate about the disk in its direction of rotation, as shown schematically in the inset in (c). (e) experimental and (f) simulated speed of the film, normalized by the average speed due to the activity far from the disk. The vertical dashed lines indicate the radius of the disk, 20 μm, and the vertical dot-dashed lines indicate the nematic correlation lengths. The alignment parameter in the simulations was $\lambda = 0.7$.

cally offers the lowest viscous resistance to flow[36]. However, the large size of the increase in flow velocity that accompanies vortex formation suggests additional factors. Specifically, we ~~interpret~~ hypothesize it ~~as~~ reflects a nonlinear rheological response of the film, in which a local region with reduced viscosity is created in response to the shear stress. This interpretation is supported by the simulations, where the viscosity terms are not stress dependent and no comparably enhanced flow velocity is observed, suggesting a need to modify existing approaches to model active nematics to capture fully their response to external stress.

~~Another consequence of~~ Further evidence for this nonlinear response is the high density of microtubule bundles in vicinity of the vortex, which as seen in Figs. 2e and 4a maintains a value characteristic of the film as a whole, leading to a point-like core. In other cases where $\mathbf{n}(\mathbf{r})$ in active nematics has adopted an azimuthal orientation, which have involved confining the active nematic through boundary conditions[24,25], the large bend distortion required of the microtubules has led to extended regions devoid of microtubules near the core. Specifically, one can identify such large empty cores of defects in the microtubule system with a regions in which the nematic order parameter is effectively reduced to zero. In conventional liquid crystals, the size of such a core region is set by a competition between the costs to the free energy of imposing large elastic distortions to the director versus converting the nematic to isotropic[36]. The large bend elastic constant of the microtubule system under ordinary conditions hence dictates that azimuthally oriented director configurations have a large empty region at the center like those ordinarily seen in Refs.[24] and[25]. In contrast, we interpret the essentially singular, point-like structure of the cores of the topological defects created by the disk, like those in Figs. 2e and 4a, as evidence that the shear-thinned region of the active nematic created by the disk has a substantially reduced bend elastic constant.

To analyze this velocity profile, we modeled the experimental conditions in fluid-dynamics calculations in COMSOL (for details see SI). The modeling characterized the low-Reynolds-number hydrodynamics due to a disk positioned at a height $d = 35$ μm above the film and rotating at $\nu = 80$ Hz to match the experimental conditions of Fig. 7. The model films behaved as quasi-2D fluids in which the velocity profile depended on the 2D viscosity η_{2D}. By varying η_{2D} to optimize agreement with the measured velocity profile, we arrived at the solid curve in Fig. 7, which corresponds to $\eta_{2D} = 1.3$ Pa·s·μm. Similar analysis of the velocity profiles around other topological vortices leads to an average viscosity for the films in the range $\eta_{2D} \approx 0.7$-5.0 Pa·s·μm.

This range of viscosities is approximately two orders of magnitude below the range found in a previous study of microtubule-based active nematics in which η_{2D} was estimated from the variation in $+1/2$ defect speed with subphase viscosity[43]. Since we identify the region of the film in vicinity of the vortex with a shear-thinned state, we expect the viscosity to be reduced. However, the difference between the measured values could also point to the problematic nature of identifying a viscosity in these out-of-equilibrium active systems. As seen with suspensions of swimming bacteria[46,47], and in contrast with conventional Newtonian fluids, different methods of measuring viscosity need not lead to the same result. We note that an additional complication in the interpretation of viscosity in active nematic films arises from the complex and not-yet fully understood coupling between activity, mechanical properties, and topological state of these systems.

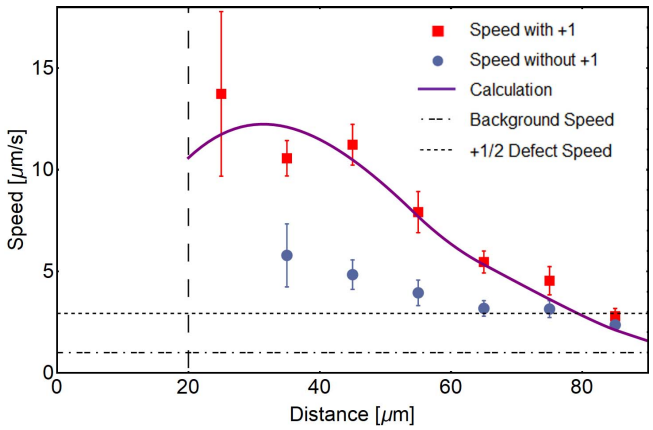

Fig. 7 Effect of topological vortex formation on the flow speed of the film. The red squares display the speed in the presence of the vortex as a function of the distance from the center of the rotating disk, while the blue circles display the speed prior to vortex formation. The horizontal dashed-dotted line indicates the average speed of microtubules in the film far from the disk due to the activity, and the dotted line displays the average speed of the $+1/2$ defects far from the disk. The vertical dashed line shows the disk radius. The solid curve shows the result of a best fit to the measured speed in the presence of the vortex, from which a film viscosity of 1.3 Pa·s·μm was obtained. The disk rotation rate was 80 Hz.

4 Conclusion

In this work we have demonstrated an original method to couple to the hydrodynamics and nematic order in an active nematic film through application of controlled stress fields and thereby to manipulate defect dynamics. This capability has allowed us to characterize rheological properties of the active system, highlighting its anomalous response to external stress. Most dramatically, this response includes a change in the topological character of the nematic, as two like-charge $+1/2$ topological defects can be drawn together to merge into a singular, point-like defect with charge $+1$. One can envision expanding this approach, for example by investigating the effects of multiple rotating disks that are either free to move in response to interactions or fixed in place. Indeed, an array of such rotating disks arranged in a lattice and coupled to the active nematic film would combine parity-breaking of the induced rotational flows with microscopic irreversibility of the activity to potentially realize novel functionalities, such as topological sound[48]. Further, when combined with approaches to affect active nematics through patterned boundary conditions[24] and other forces[39], this strategy for engineering the topology and dynamics through appropriately applied local stress fields should find application in other classes of active matter.

5 Acknowledgements

We thank P. Bose, Z. Dogic, B. Lemma, L. Lemma, and M. Ridilla for helpful discussions. We also gratefully acknowledge the NSF MRSEC at Brandeis University (DMR-1420382) for providing materials. Funding was provided by the NSF (DMR-1610875). This project has received funding (TNS) from the European Research Council (ERC) under the European Union's Horizon 2020 research and innovation programme (grant agreement No. 851196).

Conflicts of interest

There are no conflicts to declare.

Notes and references

1 A. Abrikosov, Fundamentals of the Theory of Metals, North-Holland, 1988.
2 P. Chaikin and T. Lubensky, Principles of Condensed Matter Physics, Cambridge University Press, 2000.
3 A. Fert, N. Reyren and V. Cros, Nature Reviews Materials, 2017, **2**, 17031.
4 M. C. Marchetti, J. F. Joanny, S. Ramaswamy, T. B. Liverpool, J. Prost, M. Rao and R. A. Simha, Rev. Mod. Phys., 2013, **85**, 1143–1189.
5 D. Needleman and Z. Dogic, Nature Reviews Materials, 2017, **2**, 17048.
6 D. Saintillan, Annual Review of Fluid Mechanics, 2018, **50**, 563–592.
7 K. Kawaguchi, R. Kageyama and M. Sano, Nature, 2017, **545**, 327.
8 T. B. Saw, A. Doostmohammadi, V. Nier, L. Kocgozlu, S. Thampi, Y. Toyama, P. Marcq, C. T. Lim, J. M. Yeomans and B. Ladoux, Nature, 2017, **544**, 212.
9 D. Dell'Arciprete, M. L. Blow, A. T. Brown, F. D. C. Farrell, J. S. Lintuvuori, A. F. McVey, D. Marenduzzo and W. C. K. Poon, Nature Communications, 2018, **9**, 4190.
10 Z. You, D. J. G. Pearce, A. Sengupta and L. Giomi, Phys. Rev. X, 2018, **8**, 031065.
11 Y. I. Yaman, E. Demir, R. Vetter and A. Kocabas, Nature communications, 2019, **10**, 2285.
12 C. Dombrowski, L. Cisneros, S. Chatkaew, R. E. Goldstein and J. O. Kessler, Phys. Rev. Lett., 2004, **93**, 098103.
13 D. L. Koch and G. Subramanian, Annual Review of Fluid Mechanics, 2011, **43**, 637–659.
14 H. Wioland, F. G. Woodhouse, J. Dunkel, J. O. Kessler and R. E. Goldstein, PRL, 2013, **110**, 268102.
15 J. Elgeti, R. G. Winkler and G. Gompper, Reports on Progress in Physics, 2015, **78**, 056601.
16 D. Nishiguchi, K. H. Nagai, H. Chaté and M. Sano, Phys. Rev. E, 2017, **95**, 020601.
17 V. Narayan, S. Ramaswamy and N. Menon, Science, 2007, **317**, 105–108.
18 T. Sanchez, D. T. N. Chen, S. J. DeCamp, M. Heymann and Z. Dogic, Nature, 2012, **491**, 431.
19 N. Kumar, R. Zhang, J. J. de Pablo and M. L. Gardel, Science Advances, 2018, **4**, eaat7779.
20 A. Doostmohammadi, T. N. Shendruk, K. Thijssen and J. M. Yeomans, Nature Communications, 2017, **8**, 15326.
21 A. J. Tan, E. Roberts, S. A. Smith, U. A. Olvera, J. Arteaga, S. Fortini, K. A. Mitchell and L. S. Hirst, Nature Physics, 2019, **15**, 1033–1039.
22 L. M. Lemma, S. J. DeCamp, Z. You, L. Giomi and Z. Dogic, Soft Matter, 2019, **15**, 3264–3272.
23 P. Guillamat, J. Ignés-Mullol and F. Sagués, Proceedings of the National Academy of Sciences, 2016, **113**, 5498–5502.
24 P. Guillamat, J. Ignés-Mullol and F. Sagués, Nature Communications, 2017, **8**, 564.
25 A. Opathalage, M. M. Norton, M. P. N. Juniper, B. Langeslay, S. A. Aghvami, S. Fraden and Z. Dogic, Proceedings of the National Academy of Sciences, 2019, **116**, 4788–4797.
26 M. H. Lee, C. P. Lapointe, D. H. Reich, K. J. Stebe and R. L. Leheny, Langmuir, 2009, **25**, 7976–7982.
27 R. G. Larson, The Structure and Rheology of Complex Fluids, Oxford University Press, 1999.
28 A. J. Vromans and L. Giomi, Soft Matter, 2016, **12**, 6490–6495.
29 X. Tang and J. V. Selinger, Soft Matter, 2017, **13**, 5481–5490.
30 R. A. Simha and S. Ramaswamy, Phys. Rev. Lett., 2002, **89**, 058101.
31 S. Ramaswamy, Annual Review of Condensed Matter Physics, 2010, **1**, 323–345.
32 D. Marenduzzo, E. Orlandini, M. E. Cates and J. M. Yeomans, Phys. Rev. E, 2007, **76**, 031921.
33 G. Foffano, J. S. Lintuvuori, K. Stratford, M. E. Cates and D. Marenduzzo, Phys. Rev. Lett., 2012, **109**, 028103.
34 S. P. Thampi, R. Golestanian and J. M. Yeomans, Phys. Rev. Lett., 2013, **111**, 118101.
35 T. N. Shendruk, K. Thijssen, J. M. Yeomans and A. Doostmohammadi, Phys. Rev. E, 2018, **98**, 010601.
36 P. de Gennes and J. Prost, The Physics of Liquid Crystals, Clarendon Press, 1993.
37 S. Shankar, S. Ramaswamy, M. C. Marchetti and M. J. Bowick, Phys. Rev. Lett., 2018, **121**, 108002.
38 A. Sokolov, A. Mozaffari, R. Zhang, J. J. de Pablo and A. Snezhko, Phys. Rev. X, 2019, **9**, 031014.
39 B. Martníez-Prat, J. Ignés-Mullol, J. Casademunt and F. Sagués, Nature Physics, 2019, **15**, 362–366.
40 L. Giomi, PRX, 2015, **5**, 031003.
41 S. P. Thampi, R. Golestanian and J. M. Yeomans, Phys. Rev. E, 2014, **90**, 062307.
42 A. Doostmohammadi, M. F. Adamer, S. P. Thampi and J. M. Yeomans, Nature communications, 2016, **7**, 10557.
43 P. Guillamat, J. Ignés-Mullol, S. Shankar, M. C. Marchetti and F. Sagués, PRE, 2016, **94**, 060602.
44 A. J. Vromans and L. Giomi, Soft Matter, 2016, **12**, 6490–6495.
45 S. J. DeCamp, G. S. Redner, A. Baskaran, M. F. Hagan and Z. Dogic, Nature Materials, 2015, **14**, 1110.
46 D. T. N. Chen, A. W. C. Lau, L. A. Hough, M. F. Islam, M. Gou-

lian, T. C. Lubensky and A. G. Yodh, Phys. Rev. Lett., 2007, **99**, 148302.
47 A. Sokolov and I. S. Aranson, Phys. Rev. Lett., 2009, **103**, 148101.
48 A. Souslov, B. C. van Zuiden, D. Bartolo and V. Vitelli, Nature Physics, 2017, **13**, 1091 – 1094.